

**High-order harmonic generation in semiconductors driven at near- and mid-infrared wavelengths**David Freeman<sup>1</sup>\* and Anatoli Kheifets<sup>2</sup>*Research School of Physics, Australian National University, Canberra, Australian Capital Territory, 2601, Australia*Shunsuke Yamada<sup>3</sup>, Atsushi Yamada<sup>3</sup>, and Kazuhiro Yabana<sup>3</sup>*Center for Computational Sciences, University of Tsukuba, Tsukuba 305-8577, Japan* (Received 17 September 2021; revised 21 July 2022; accepted 2 August 2022; published 19 August 2022)

We study high-order harmonics generation (HHG) in crystalline silicon and diamond subjected to near- and mid-infrared laser pulses. We employ time-dependent density functional theory and solve the time-dependent Kohn-Sham equation in the single-cell geometry. We demonstrate that clear and clean HHG spectra can be generated with careful selection of the pulse duration. In addition, we simulate dephasing effects in a large silicon supercell through a displacement of atomic positions prepared by a molecular dynamics simulation. We compare our results with the previous calculations by Floss *et al.* [*Phys. Rev. A* **97**, 011401(R) (2018)] on diamond at 800 nm and by Tancogne-Dejean *et al.* [*Phys. Rev. Lett.* **118**, 087403 (2017)] on Si at 3000 nm.

DOI: [10.1103/PhysRevB.106.075202](https://doi.org/10.1103/PhysRevB.106.075202)**I. INTRODUCTION**

High-order harmonics generation (HHG) in solids has attracted efforts of many experimental and theoretical groups. The ultimate goal of these efforts is producing a compact and tunable source of coherent extreme ultraviolet and soft X-rays on a chip that can be integrated into a microelectronic device. The recent advances of HHG in solids has been reviewed in the experiment [1] and theory [2]. Previous efforts on HHG in condensed matter have been driven by improved harmonic intensities offered by the higher atomic densities of solids compared to those offered by atomic gases. Experimental studies into HHG for thin films of bulk crystal targets [3–13] have shown that improved intensities are achievable as demonstrated theoretically [1]. Targets have also recently been expanded to structured metasurfaces [14,15] and their two-dimensional component layers, such as graphene [16–18].

Theoretical studies currently employ methods of varying quantitative power to model the interaction of solid-state targets with the pulsed electric fields driving HHG. These methods include solution of the time-dependent Schrödinger equation [19–21], one-dimensional models [22–26], density matrix models [27–29], and *ab initio* descriptions, such as time-dependent density functional theory (TDDFT) [30–34]. Recently, theories have also been developed to describe HHG in more complex targets, such as bulk surfaces [35–37] and metasurfaces [38]. Investigations using these methods have revealed the contribution of inter- and intraband mechanisms of the HHG process which are visualized in the energy band picture [1,28]. Similarly, the impact of band structure, band selection, and laser polarization have been studied at length theoretically [8,10,17].

The theoretical description of HHG in bulk crystalline targets requires dealing with light propagation effects. Indeed, in the experiment, a strong dephasing effect is often observed for condensed-matter targets [5,6,10,28,39,40]. This effect has been explored in theoretical studies [31,32,41] and found to be prominent in bulk solids due to the higher atomic density than found in atomic gases. However, ultrafast dephasing times on the order of 1 fs that has been proposed in theory [42,43] have posed a problem for the strong-field community. Recently, these dephasing times have been reconsidered through simulation of the linear response of the current density to broadband excitation [31]. This analysis proposed dephasing times on the order of 10 fs and rectified the experimental and theoretical spectra generated using TDDFT and semiconductor Bloch equations (SBE) through simulation of the laser focus propagation effect.

One of the major goals of theoretical investigations of HHG in solids is to find the optimum conditions to generate clear and strong harmonic signals. In the Maxwell-SBE calculations [31], it was shown that the propagation effect is essential to obtain a clear HHG signal of high order due to the dephasing effect. Using the single-scale Maxwell-TDDFT scheme [44], an effort was made to find the optimal thickness of a thin film that produces the most intense HHG signals. It was shown that a very thin film of thickness of 2–15 nm is the optimum choice to produce intense HHG signals. In the present paper, we investigate yet another unexplored factor, a time duration of the pulse that produces clear and intense HHG signals of high order. For longer driving pulses, more cycles near the maximum field strength contribute to the HHG process with the matter current getting closer to a quasiperiodic behavior, thus, contributing to cleaner harmonic peaks. For the purpose of our investigation, we study HHG in crystalline diamond (Di) and Si utilizing the TDDFT implementation within the computational scalable *ab initio* light-matter simulator for optics

\*david.freeman@anu.edu.au

and nanoscience (SALMON) framework [45]. We limit ourselves with the single cell (SC) calculations, which solve the time-dependent Kohn-Sham (TDKS) equation for the electron dynamics in TDDFT. These calculations consider the interaction between the electrons inside the bulk crystal targets and a prespecified pulsed electric field. Within this scheme, we also investigate a dephasing effect by considering a large supercell with thermally distorted atomic positions. Calculation of HHG signals from the supercell will clarify the dephasing effect coming from electron-phonon coupling.

The paper is organized as follows: In Sec. II we describe the theoretical techniques for both time-dependent HHG and dephasing calculations. In Sec. III, we present numerical results and examine the HHG spectra. We conclude in Sec. IV by outlining the future of this method through extension to other condensed-matter systems.

## II. METHODS

### A. Single unit-cell method

The SC-TDDFT method considers the interaction of a bulk crystal unit cell with a spatially uniform electric field [46,47]. This method has been used in the study of nonlinear and ultrafast dynamics [30–34,48–52]. Utilizing the dipole approximation, the electronic motion can be described through the Bloch orbitals of the bulk,  $u_{nk}(\mathbf{r}, t)$  where the wave-vector  $\mathbf{k}$  is contained within the three-dimensional (3D) Brillouin zone of the bulk solid. The TDKS equation for such orbitals is written as

$$i\hbar \frac{\partial u_{nk}(\mathbf{r}, t)}{\partial t} = \left\{ \frac{1}{2m} \left[ -i\hbar \nabla + \hbar \mathbf{k} + \hat{\mathbf{x}} \frac{e}{c} A(t) \right]^2 - e\phi(\mathbf{r}, t) + \delta \hat{V}_{\text{ion}} + V_{xc}(\mathbf{r}, t) \right\} u_{nk}(\mathbf{r}, t). \quad (1)$$

The applied electric field in this approach is defined by the vector potential of the incident pulse  $A(t)$ . The electric potential  $\phi(\mathbf{r}, t)$  includes the Hartree potential from the electrons and the local contribution of the ionic potential. The terms  $\delta V_{\text{ion}}$  and  $V_{xc}(\mathbf{r}, t)$  describe the nonlocal part of the ionic pseudopotential [53] and the exchange-correlation potential [54], respectively. In our calculations, this exchange-correlation potential utilizes the adiabatic local-density approximation (LDA) [55]. Note that the LDA underestimates the band gap of Si, as it does for diamond and other dielectrics. The experimental direct band gap of Si is 3.4 eV whereas LDA gives 2.4 eV. We neglect the exchange-correlation term in the vector potential  $A_{xc}(t)$  for simplicity and do not rigorously model the exchange-correlation effects of these types for infinite periodic systems [56,57].

The averaged electric current density, used in generating HHG spectra, is calculated as follows:

$$\mathbf{J}(t) = -\frac{e}{m} \int_{\Omega} \frac{d\mathbf{r}}{\Omega} \sum_{nk}^{\text{occ}} u_{nk}(\mathbf{r}, t) \times \left( -i\hbar \nabla + \hbar \mathbf{k} + \hat{\mathbf{x}} \frac{e}{c} A(t) \right) u_{nk}(\mathbf{r}, t) + \delta \mathbf{J}(t). \quad (2)$$

Here  $\Omega$  is the volume of the unit cell and  $n$  is the band index restricted to occupied bands. The term  $\delta \mathbf{J}(t)$  denotes the contribution to the current density from the nonlocal part of the pseudopotential [46] and is given as follows:

$$\delta \mathbf{J}(t) = -\frac{e}{m} \int \frac{d\mathbf{r}}{\Omega} \sum_{nk}^{\text{occ}} u_{nk}^*(\mathbf{r}, t) e^{-i[\mathbf{k} + \hat{\mathbf{x}}(e/c)A(t)]\mathbf{r}} \times \frac{[\mathbf{r}, \delta \hat{V}_{\text{ion}}]}{i\hbar} e^{i[\mathbf{k} + \hat{\mathbf{x}}(e/c)A(t)]\mathbf{r}} u_{nk}(\mathbf{r}, t). \quad (3)$$

### B. Simulation details

We utilize the open-source software package SALMON [45]. In this code, a uniform 3D spatial grid is defined for the electron orbitals. The time evolution of the electron orbitals is carried out using the Taylor expansion method [58].

For TDDFT calculations without dephasing, we define a cubic unit cell of the diamond structure containing eight atoms with varying side lengths depending on the specific target. For Di and Si calculations, the unit-cell dimensions are defined as  $a_{\text{Di}} = 0.357$  and  $a_{\text{Si}} = 0.543$  nm. A spatial grid of  $16^3$  points is used in Si and  $24^3$  in Di calculations to enable an accurate description of the Bloch orbitals. Convergence over spatial ( $r$ -point) grids is observed at these grid sizes. Similarly, the 3D Brillouin zone is sampled by a grid made up of  $32^3$   $k$  points. Note that convergence over the Brillouin zone is not observed at this grid size for diamond although qualitatively this size appears reasonable where we restrict ourselves to below the 50th-order harmonic. Otoabe [30] finds similar grid parameters for diamond but with convergence observed over the Brillouin zone. The time step is set for stability of the calculation to be  $2.5 \times 10^{-3}$  fs for Si and  $1 \times 10^{-3}$  fs for Di. Note that tests for convergence are important in these calculations due to the discretization of the spatial,  $k$  space and time parameters discussed here.

For the Si calculation with dephasing, a supercell of size  $4^3$  describing a 512 atom system is used. The Brillouin zone is sampled by a grid made up of  $8^3$   $k$  points. Atomic positions are shifted from the equilibrium position with the diamond structure whereas are frozen during the time evolution of electron orbitals. They are generated from molecular dynamics simulations. The detail of the preparation will be described below.

### C. Generating HHG spectra

In our SC-TDDFT calculations, we utilize the following incident pulse profile:

$$A(t) = -\frac{cE_0}{\omega} \sin(\omega t) \cos^6 \left[ \frac{\pi}{T} \left( t - \frac{T}{2} \right) \right], \quad 0 \leq t \leq T. \quad (4)$$

Here  $E_0$  is the peak amplitude of the electric field,  $\omega$  is the carrier frequency, and  $T$  is the full duration of the pulse. For the  $\cos^6$  envelope, the full width at half maximum (FWHM) duration  $T_{\text{FWHM}}$  is related to the full duration  $T$  by  $T_{\text{FWHM}} \simeq 0.3T$ . In our calculations, we consider the photon energies  $\hbar\omega = 0.43$  eV ( $\lambda = 3000$  nm),  $\hbar\omega = 0.62$  eV ( $\lambda = 2000$  nm) or  $\hbar\omega = 1.55$  eV ( $\lambda = 800$  nm). We select typical pulse durations  $T \gtrsim 100$  fs which are considerably larger than in

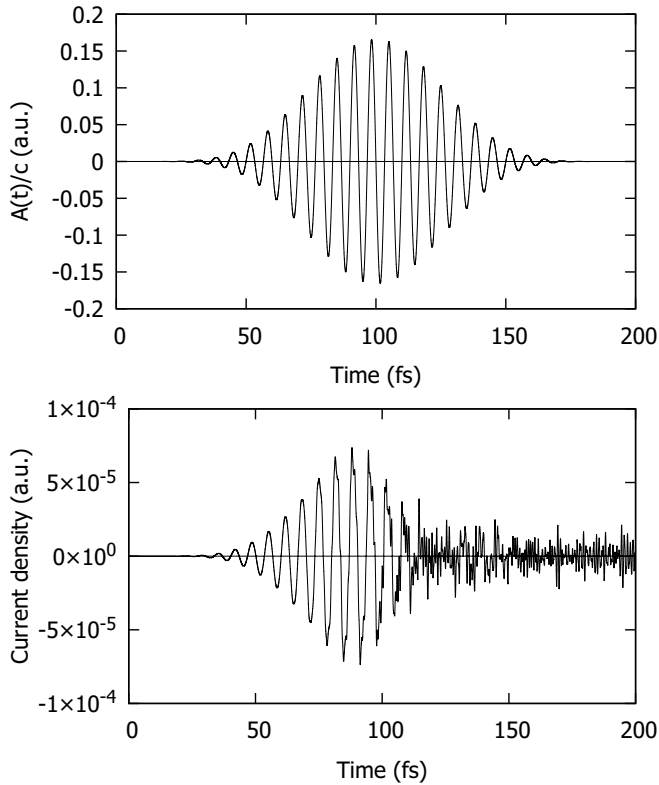


FIG. 1. The applied vector potential (top) of a pulse with a full duration of 200 fs at  $\lambda = 2000$  nm and the peak intensity  $5 \times 10^{11}$  W/cm<sup>2</sup> and the matter current (bottom) in Si from a SC-TDDFT simulation.

previous HHG studies ( $\sim 32$  fs in Refs. [31,32] and 30 fs in Ref. [44]).

In the SC-TDDFT formalism, the HHG spectrum is calculated as a Fourier transform of the matter current,

$$\text{HHG}(\omega) = \omega^2 |J(\omega)|^2, \quad (5)$$

$$J(\omega) = \int dt e^{i\omega t} J(t) w(t), \quad (6)$$

$$w(t) = 1 - \left(\frac{t}{T}\right)^2 + 2\left(\frac{t}{T}\right)^3, \quad (7)$$

where  $w(t)$  is the window smoothing function applied to remove spurious peaks in the spectra. A Gaussian convolution of the form

$$\text{HHG}_{\text{av}}(\omega) = \int d\omega' (\pi\epsilon^2)^{-1/2} \exp\left[-\left(\frac{\omega - \omega'}{\epsilon^2}\right)^2\right] \text{HHG}(\omega') \quad (8)$$

is applied to carry out frequency averaging as often the case in experimental HHG measurements.

### III. RESULTS

#### A. Bulk Si at mid-IR wavelengths

We first consider bulk Si driven by a 2000-nm laser pulse with 200-fs full duration and a peak intensity of  $5 \times 10^{11}$  W/cm<sup>2</sup>. In Fig. 1, the time profile of the vector potential is shown in the upper panel, and the induced mat-

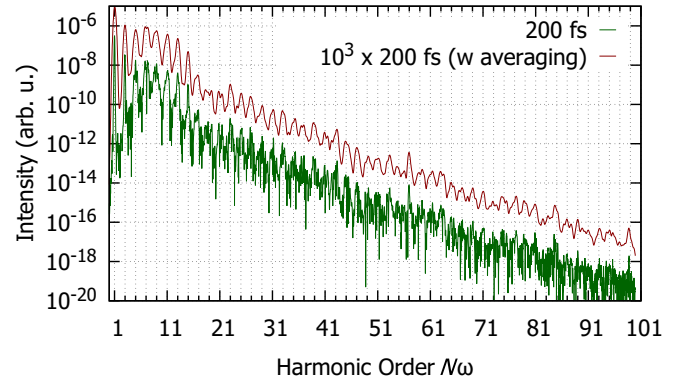


FIG. 2. HHG spectra for Si are generated with a Fourier transform (green) and then Gaussian convolution (red) using Eq. 8 with  $\epsilon = 0.136$  eV. The spectra are the result of SC-TDDFT calculation considering interaction with a pulse with a full duration of 200 fs at  $\lambda = 2000$  nm and peak intensity  $5 \times 10^{11}$  W/cm<sup>2</sup>.

ter current is shown in the lower panel. Here the simulated matter current displays large noise contributions that become particularly prominent after around 110 fs. Note also that the current is very asymmetric compared to the symmetric driving pulse centered around 100 fs. We, thus, find that the SC-TDDFT method assuming a diamond structure without any distortion effects records unphysically oscillating current towards the end of the specified pulse length. In Sec. III C, we will show that the oscillating current mostly disappears once we introduce the dephasing effect caused by the thermal motion of atoms.

Figure 2 displays the corresponding HHG spectrum (in green) generated from the matter current shown in Fig. 1 using Eqs. (5)–(7). We confirmed the simulation's convergence over spatial ( $r$ -point) and momentum ( $k$ -point) grids up to 51st-order harmonic for Si at 2000 nm. Nevertheless we show the spectrum up to 99th order to demonstrate both the presence of, and our methods application to, higher-order harmonics. Although HHG signals can be identified in the unaltered spectrum (green) even around the highest order shown in the figure, the harmonic structure appears noisy and some harmonics cannot be clearly seen in this spectrum. Gaussian convolution using Eq. (8) overcomes this problem. Figure 2 shows the spectrum with the Gaussian filter (in red).

Figure 3 demonstrates the major effect that pulse duration has on the clarity and extent of HHG spectra, considering a 3000-nm pulse interacting with Si. The 200-fs calculation (in green) shows clear harmonic peaks beyond the 27th harmonic order where the 70-fs calculation generally shows unclear harmonics until the 15th order. In addition to this, we note that the harmonic cutoff, comparing the simulations for the 200- and 70-fs pulses appears dependent on pulse duration. We further examined this dependence through the application of an inverse Gabor transform focused to reveal the underlying current contributions associated with the highest-order harmonics. Our analysis demonstrates as expected, the importance of multicycle current accumulation in the formation of harmonic structure, where we observe that a 70-fs 3000-nm pulse possesses too few cycles to capture the higher-order returns.

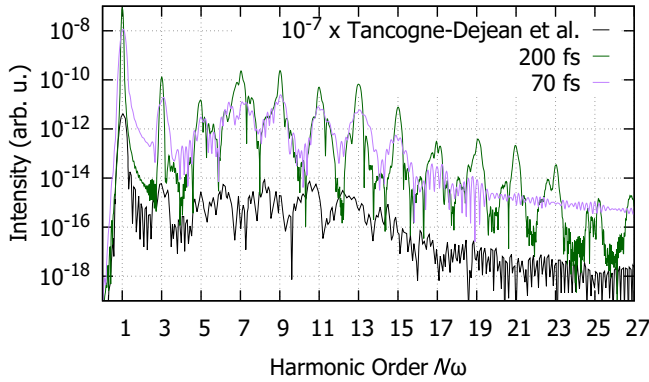


FIG. 3. HHG spectra for Si are generated with a Fourier transform (green) and compared with calculation (purple) similar to Tancogne-Dejean *et al.* [34] (black). The spectra are the result of SC-TDDFT calculation considering interaction with a pulse with full durations of 200 and 70 fs, respectively, at  $\lambda = 3000$  nm and peak intensity  $1 \times 10^{11}$  W/cm<sup>2</sup>. Note that a  $\cos^6$  envelope is applied here (for the pink calculation) instead of the  $\cos^2$  carrier used by Tancogne-Dejean *et al.* [34].

Our Si results at 2000 nm (Fig. 2) and 3000 nm (Fig. 3) need to be contrasted with the earlier calculation on Si at 3000 nm presented by Tancogne-Dejean *et al.* [34]. In particular, using equivalent parameters to those reported in Ref. [34], a direct comparison is achieved for 3000 nm in Fig. 3. Tancogne-Dejean *et al.* [34] recorded noisy harmonics of the lower order whereas their higher-order harmonics appeared clean. They related this effect with the joint density of states (JDOS) as a measure of the overlap between the valence and the conduction bands. A large overlap and high JDOS would promote the recombination and interband HHG. Somewhat counterintuitively, Tancogne-Dejean *et al.* [34] discovered that a high JDOS was in fact detrimental to HHG emission making the corresponding harmonic peaks noisy. Conversely, those harmonics falling into a low JDOS region of the HHG spectrum stayed clean. This observation led the authors to conclude that it was the intraband mechanism that was largely responsible for HHG in silicon driven at mid-IR (MIR). However, our HHG spectra at both 2000 nm (Fig. 2) and 3000 nm (Fig. 3) at 200-fs total duration are both entirely clean even without averaging. Note that we do not observe a clear and obvious JDOS effect in our calculations at both 2000 and 3000 nm when the pulse duration is sufficiently large.

### B. Bulk diamond at near IR wavelengths

In Fig. 4 we display the HHG spectra of Di produced by the SC-TDDFT. The primary calculation is driven by an 800-nm incident pulse of a 200-fs full duration and the peak intensity of  $1 \times 10^{13}$  W/cm<sup>2</sup>. The Gaussian convoluted spectrum again reveals clear harmonics up to 41st order of the fundamental frequency  $\omega$ , shown in the top panel of Fig. 4. The lower-order harmonics of this spectrum are zoomed in on the bottom panel. The HHG spectrum is compared with an analogous calculation of Floss *et al.* [32]. The three sets of the SC-TDDFT calculations displayed in Fig. 4 are clearly differentiated by the pulse duration.

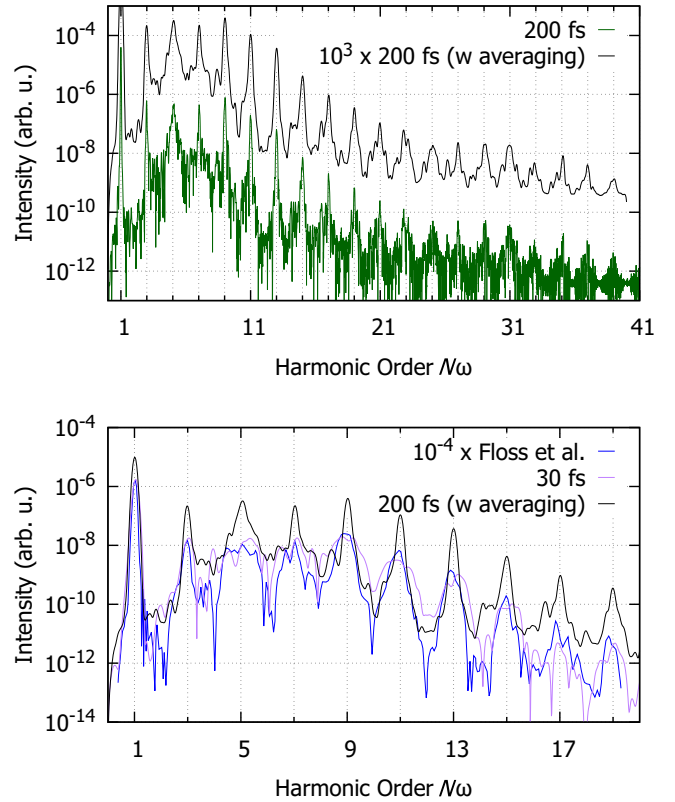


FIG. 4. Top: The HHG spectrum of Di (shown in green) and Gaussian convoluted spectrum (in black), using Eq. (80 with  $\epsilon = 0.136$  eV, are generated with SC-TDDFT driven by a 800-nm pulse with a full duration of 200 fs and the peak intensity of  $1 \times 10^{13}$  W/cm<sup>2</sup>. Bottom: The analogous spectrum of Floss *et al.* [32] with dephasing is displayed in blue and an SC-TDDFT calculation for a 32-fs pulse is shown in purple. The top and bottom panels show the expanded and zoomed in low-order HHG spectra, respectively.

These authors employed the SC-TDDFT driven by a  $2 \times 10^{13}$  W/cm<sup>2</sup> pulse with a total duration of 32 fs [31]. Such a calculation did not produce a particularly clear HHG spectrum as is seen in Fig. 4. It is only the Maxwell propagation technique coupled with the SBE that allowed Floss *et al.* [31] to generate a clear spectrum. We, thus, conclude that with refined parameters and a longer pulse duration, one can obtain distinguishable high harmonics within the SC-TDDFT alone, whereas in previous calculations [32] the Maxwell propagation or an inclusion of the explicit dephasing effect was required to obtain clear spectra that are often observed in measurements.

### C. Dephasing effect

We expand the SC-TDDFT method to consider the atomic system at a finite temperature by allowing the atomic positions to be displaced from equilibrium. For this purpose, we consider bulk Si and first carry out a molecular dynamics simulation with an empirical force field at a specified temperature using a thermostat. We use LAMMPS software [59] to carry out the molecular dynamics simulation where a three-body Stillinger-Weber potential [60] is used. We pick up several atomic configurations with sufficiently long intervals and use

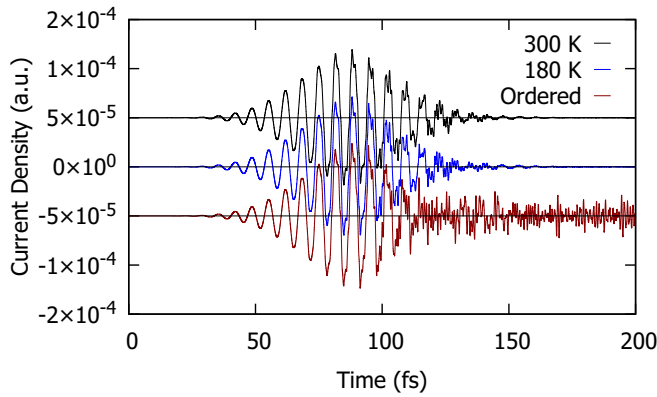


FIG. 5. Examples of the dephasing effect on the matter current in Si that arises from the application of a mean atomic position distortion. An effective temperature of 180 K (300 K) is used in simulating the current density shown in blue (black). These examples consider a 200-fs full duration pulse impinging on bulk Si and are compared to current from a similar TDDFT calculation without distortion of atomic positions (red). A shift of  $5 \times 10^{-5}$  is applied to help distinguish these results.

these configurations in the SC-TDDFT. This represents a first-principles approach introducing the dephasing effect into TDDFT without relying on phenomenological parameter  $T_2$ . This is a convenient approach where we consider that previously ultrafast dephasing times  $T_2 \sim 1$  fs had to be introduced to reconcile theoretical treatments and experiment. During the time-evolution stage in the SC-TDDFT, the atomic positions are fixed. We carry out calculations using supercells of different sizes and have found that results of different configurations are quite similar to each other if we choose sufficiently large supercell. We will show below the calculation results using a supercell containing 512 atoms. Employing  $8^3$   $k$  points, the total number of atoms is equal to 262 and 144, that is equal to the total number of atoms in a cell containing eight atoms with the  $32^3$   $k$  points that we showed in Fig. 2. In fact, we numerically confirmed that calculations without any distortion coincide with each other accurately between the two unit cells, eight atoms with  $32^3$   $k$  points and 512 atoms with  $8^3$   $k$  points.

We show electron current density in bulk Si under the applied electric field in Fig. 5, caused by the same applied pulse as shown in Fig. 1. The black (blue) calculation displays the current under the atomic configuration at a temperature of 300 K (180 K). The matter current in disordered Si with distortion exhibits the desired dephasing after the pulse has ceased interacting. With dephasing present, signals beyond 150 fs appear significantly suppressed and the noise contributions seen in Fig. 1 (red in Fig. 5) are removed.

Figure 6 demonstrates the effect of incorporating dephasing into the HHG calculations in Si where Gaussian convolutions are also applied. The black calculation shows the HHG spectrum using atomic positions from a molecular dynamics calculation at 300 K. Whereas signals up to 100th order can be seen in Fig. 2 without atomic distortion, here we can see HHG signals up to 31st order, and higher-order signals cannot be identified. We also note that the HHG signals themselves become deeper between peaks and cleaner than those without atomic distortion even when not incor-

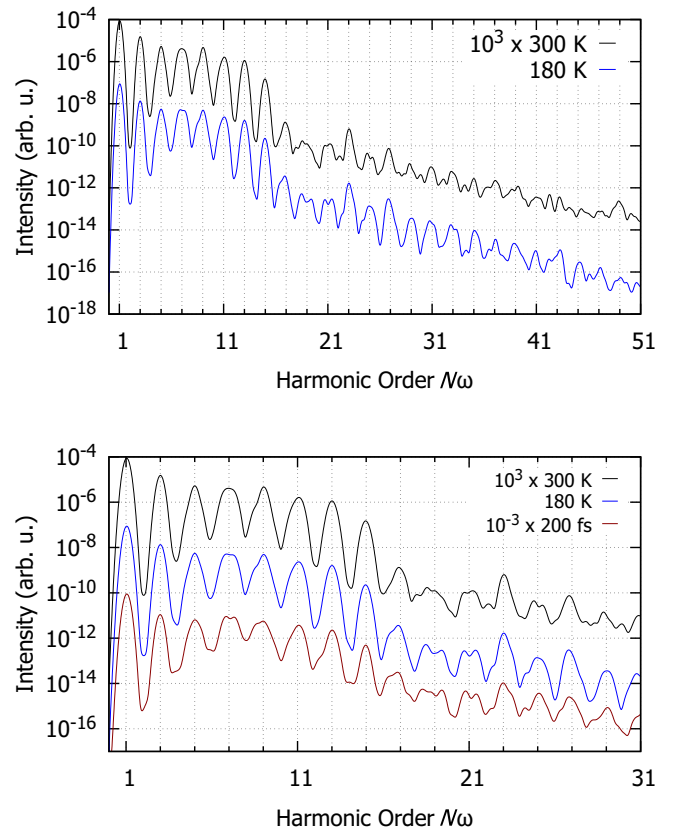


FIG. 6. Comparison of convoluted HHG spectra from bulk Si with dephasing effect by an atomic displacement (top), together with its equivalent single-cell calculation (red, bottom) with Gaussian convolution applied using Eq. (8) with  $\epsilon = 0.136$  eV. Blue and black calculations here show the convoluted spectrum with atomic displacement by a thermal motion at 180 K (300 K) in classical molecular dynamics calculation.

porating a Gaussian convolution. Therefore, the dephasing effect modified the HHG spectrum in two ways, removing signals of HHG signals higher than 31st order, and increasing peak-to-peak depth for those signals that survive.

In Fig. 6, the blue calculation shows the HHG spectrum using atomic positions from a molecular dynamics simulation at 180 K. Now we find HHG signals up to the 49th order, where higher-order signals are suppressed. This result at 180 K clearly indicates that it is important to keep the material cold in measuring HHG to observe higher-order signals. We, however, note that the distortion of atomic positions is generated by the classical molecular dynamics calculation. At very low temperatures, quantum zero-point motion will contribute significantly and should be included in discussing the HHG spectra.

The results with the effective thermally induced dephasing effect, incorporated through atomic positions generated by molecular dynamics simulations, suggest that sample cooling could be used to greatly improve the high-order harmonic signal intensity observed in experiment. In principle, this should not pose a problem to current experiment as liquid nitrogen or helium cooling is commonly utilized in a variety of condensed-matter physics contexts.

It should be noted that we have opted to consider fixed ionic coordinates in our dephasing simulations instead of performing evolution through classical mechanics. We do not incorporate an Ehrenfest molecular dynamics approach into TDDFT as we consider that spurious coherence may occur in the classical approximation when considering solids as, when one considers molecules, the coherence between two states will soon disappear as the ionic wave packets evolve differently between ionized and nonionized electronic states and the spurious coherence that may occur in molecular simulations could extend to simulations concerning solids.

#### IV. CONCLUDING REMARKS

We have presented here clear HHG spectra for diamondlike semiconductors interacting with near- and mid-IR pulsed electric fields. We obtain clear harmonic spectra for sufficiently long pulses with durations  $T_{\text{FWHM}} \gtrsim 70$  fs and these spectra are further clarified through Gaussian convolution. We, therefore, review the suggestions made in previous literature considering diamond [31,32] and silicon [34]. In crystalline

Si, we do not observe the expected joint density of states effect but do demonstrate a prominent dephasing effect on the HHG spectra. Using a first-principles approach introducing dephasing into TDDFT we observe that higher-order harmonics are strongly suppressed by the decoherence effects in the target whereas lower-order harmonics appear clearer in the spectra. On the basis of the strength of the decoherence effects for Si at 2000-nm laser wavelengths, we suggest that helium or liquid nitrogen cooling of the target will improve higher-order harmonic intensity returns.

#### ACKNOWLEDGMENTS

We acknowledge the two supercomputer resources employed for TDDFT calculations: the National Computational Infrastructure (NCI Australia) and Fugaku at RIKEN R-CCS, Japan, with support through the HPCI System Research Project (Project No. hp210137). This research was partially supported by JST-CREST under Grant No. JP-MJCR16N5, by MEXT Quantum Leap Flagship Program (MEXT Q-LEAP) under Grant No. JPMXS0118068681, and by JSPS KAKENHI Grant No. 20H02649.

- 
- [1] S. Ghimire and D. A. Reis, High-harmonic generation from solids, *Nat. Phys.* **15**, 10 (2019).
- [2] C. Yu, S. Jiang, and R. Lu, High order harmonic generation in solids: a review on recent numerical methods, *Adv. Phys.: X* **4**, 1562982 (2019).
- [3] S. Ghimire, A. D. DiChiara, E. Sistrunk, P. Agostini, L. F. DiMauro, and D. A. Reis, Observation of high-order harmonic generation in a bulk crystal, *Nat. Phys.* **7**, 138 (2011).
- [4] O. Schubert, M. Hohenleutner, F. Langer, B. Urbanek, C. Lange, U. Huttner, D. Golde, T. Meier, M. Kira, S. W. Koch *et al.*, Sub-cycle control of terahertz high-harmonic generation by dynamical Bloch oscillations, *Nat. Photonics* **8**, 119 (2014).
- [5] M. Hohenleutner, F. Langer, O. Schubert, M. Knorr, U. Huttner, S. W. Koch, M. Kira, and R. Huber, Real-time observation of interfering crystal electrons in high-harmonic generation, *Nature (London)* **523**, 572 (2015).
- [6] T. T. Luu, M. Garg, S. Y. Kruchinin, A. Moulet, M. T. Hassan, and E. Goulielmakis, Extreme ultraviolet high-harmonic spectroscopy of solids, *Nature (London)* **521**, 498 (2015).
- [7] G. Vampa, T. J. Hammond, N. Thiré, B. E. Schmidt, F. Légaré, C. R. McDonald, T. Brabec, and P. B. Corkum, Linking high harmonics from gases and solids, *Nature (London)* **522**, 462 (2015).
- [8] F. Langer, M. Hohenleutner, U. Huttner, S. W. Koch, M. Kira, and R. Huber, Symmetry-controlled time structure of high-harmonic carrier fields from a solid, *Nat. Photonics* **11**, 227 (2017).
- [9] H. Liu, Y. Li, Y. S. You, S. Ghimire, T. F. Heinz, and D. A. Reis, High-harmonic generation from an atomically thin semiconductor, *Nat. Phys.* **13**, 262 (2017).
- [10] Y. S. You, D. A. Reis, and S. Ghimire, Anisotropic high-harmonic generation in bulk crystals, *Nat. Phys.* **13**, 345 (2017).
- [11] H. Shirai, F. Kumaki, Y. Nomura, and T. Fuji, High-harmonic generation in solids driven by subcycle midinfrared pulses from two-color filamentation, *Opt. Lett.* **43**, 2094 (2018).
- [12] G. Vampa, T. J. Hammond, M. Taucer, X. Ding, X. Ropagnol, T. Ozaki, S. Delprat, M. Chaker, N. Thiré, B. E. Schmidt *et al.*, Strong-field optoelectronics in solids, *Nat. Photonics* **12**, 465 (2018).
- [13] G. Orenstein, A. J. Uzan, S. Gadasi, T. Arusi-Parpar, M. Krüger, R. Cireasa, B. D. Bruner, and N. Dudovich, Shaping electron-hole trajectories for solid-state high harmonic generation control, *Opt. Express* **27**, 37835 (2019).
- [14] A. Krasnok, M. Tymchenko, and A. Alù, Nonlinear metasurfaces: a paradigm shift in nonlinear optics, *Mater. Today* **21**, 8 (2018).
- [15] H. Liu, C. Guo, G. Vampa, J. L. Zhang, T. Sarmiento, M. Xiao, P. H. Bucksbaum, J. Vukovi, S. Fan, and D. A. Reis, Enhanced high-harmonic generation from an all-dielectric metasurface, *Nat. Phys.* **14**, 1006 (2018).
- [16] N. Yoshikawa, T. Tamaya, and K. Tanaka, High-harmonic generation in graphene enhanced by elliptically polarized light excitation, *Science* **356**, 736 (2017).
- [17] N. Yoshikawa, K. Nagai, K. Uchida, Y. Takaguchi, S. Sasaki, Y. Miyata, and K. Tanaka, Interband resonant high-harmonic generation by valley polarized electron-hole pairs, *Nat. Commun.* **10**, 3709 (2019).
- [18] H. A. Hafez, S. Kovalev, J.-C. Deinert, Z. Mics, B. Green, N. Awari, M. Chen, S. Germanskiy, U. Lehnert, J. Teichert, *et al.*, Extremely efficient terahertz high-harmonic generation in graphene by hot Dirac fermions, *Nature (London)* **561**, 507 (2018).
- [19] M. Wu, S. Ghimire, D. A. Reis, K. J. Schafer, and M. B. Gaarde, High-harmonic generation from Bloch electrons in solids, *Phys. Rev. A* **91**, 043839 (2015).

- [20] T. Apostolova and B. Obreshkov, Ultrafast photoionization and excitation of surface-plasmon-polaritons on diamond surfaces, *Diam. Relat. Mater.* **82**, 165 (2018).
- [21] C. W. Byun, M.-H. Lee, and N. N. Choi, High-order harmonic generation from solids using houston states, *J. Korean Phys. Soc.* **78**, 662 (2021).
- [22] K. K. Hansen, T. Deffge, and D. Bauer, High-order harmonic generation in solid slabs beyond the single-active-electron approximation, *Phys. Rev. A* **96**, 053418 (2017).
- [23] T. Ikemachi, Y. Shinohara, T. Sato, J. Yumoto, M. Kuwata-Gonokami, and K. L. Ishikawa, Trajectory analysis of high-order-harmonic generation from periodic crystals, *Phys. Rev. A* **95**, 043416 (2017).
- [24] D. Bauer and K. K. Hansen, High-Harmonic Generation in Solids with and without Topological Edge States, *Phys. Rev. Lett.* **120**, 177401 (2018).
- [25] K. K. Hansen, D. Bauer, and L. B. Madsen, Finite-system effects on high-order harmonic generation: From atoms to solids, *Phys. Rev. A* **97**, 043424 (2018).
- [26] J.-Z. Jin, H. Liang, X.-R. Xiao, M.-X. Wang, S.-G. Chen, X.-Y. Wu, Q. Gong, and L.-Y. Peng, Contribution of floquet-bloch states to high-order harmonic generation in solids, *Phys. Rev. A* **100**, 013412 (2019).
- [27] S. Ghimire, A. D. DiChiara, E. Sistrunk, G. Ndashimiye, U. B. Szafruga, A. Mohammad, P. Agostini, L. F. DiMauro, and D. A. Reis, Generation and propagation of high-order harmonics in crystals, *Phys. Rev. A* **85**, 043836 (2012).
- [28] G. Vampa, C. R. McDonald, G. Orlando, D. D. Klug, P. B. Corkum, and T. Brabec, Theoretical Analysis of High-Harmonic Generation in Solids, *Phys. Rev. Lett.* **113**, 073901 (2014).
- [29] G. Vampa, C. R. McDonald, G. Orlando, P. B. Corkum, and T. Brabec, Semiclassical analysis of high harmonic generation in bulk crystals, *Phys. Rev. B* **91**, 064302 (2015).
- [30] T. Otobe, First-principle description for the high-harmonic generation in a diamond by intense short laser pulse, *J. Appl. Phys.* **111**, 093112 (2012).
- [31] I. Floss, C. Lemell, G. Wachter, V. Smejkal, S. A. Sato, X.-M. Tong, K. Yabana, and J. Burgdörfer, *Ab initio* multiscale simulation of high-order harmonic generation in solids, *Phys. Rev. A* **97**, 011401(R) (2018).
- [32] I. Floss, C. Lemell, K. Yabana, and J. Burgdörfer, Incorporating decoherence into solid-state time-dependent density functional theory, *Phys. Rev. B* **99**, 224301 (2019).
- [33] T. Otobe, High-harmonic generation in alpha-quartz by electron-hole recombination, *Phys. Rev. B* **94**, 235152 (2016).
- [34] N. Tancogne-Dejean, O. D. Mücke, F. X. Kärtner, and A. Rubio, Impact of the Electronic Band Structure in High-Harmonic Generation Spectra of Solids, *Phys. Rev. Lett.* **118**, 087403 (2017).
- [35] A. T. Georges and N. E. Karatzas, Theory of multiple harmonic generation in reflection from a metal surface, *Appl. Phys. B: Lasers Opt.* **81**, 479 (2005).
- [36] D. Golde, T. Meier, and S. W. Koch, High harmonics generated in semiconductor nanostructures by the coupled dynamics of optical inter- and intraband excitations, *Phys. Rev. B* **77**, 075330 (2008).
- [37] G. Le Breton, A. Rubio, and N. Tancogne-Dejean, High-harmonic generation from few-layer hexagonal boron nitride: Evolution from monolayer to bulk response, *Phys. Rev. B* **98**, 165308 (2018).
- [38] M. R. Shcherbakov, K. Werner, Z. Fan, N. Talisa, E. Chowdhury, and G. Shvets, Photon acceleration and tunable broadband harmonics generation in nonlinear time-dependent metasurfaces, *Nat. Commun.* **10**, 1345 (2019).
- [39] T. T. Luu and H. J. Wörner, High-order harmonic generation in solids: a unifying approach, *Phys. Rev. B* **94**, 115164 (2016).
- [40] C. Yu, X. Zhang, S. Jiang, X. Cao, G. Yuan, T. Wu, L. Bai, and R. Lu, Dependence of high-order-harmonic generation on dipole moment in SiO<sub>2</sub> crystals, *Phys. Rev. A* **94**, 013846 (2016).
- [41] G. Orlando, T.-S. Ho, and S.-I. Chu, Simple model of dephasing for high-order harmonic generation in solids, *J. Opt. Soc. Am. B* **37**, 1540 (2020).
- [42] Y. W. Kim, T.-J. Shao, H. Kim, S. Han, S. Kim, M. Ciappina, X.-B. Bian, and S.-W. Kim, Spectral interference in high harmonic generation from solids, *ACS Photonics* **6**, 851 (2019).
- [43] T.-Y. Du, Probing the dephasing time of crystals via spectral properties of high-order harmonic generation, *Phys. Rev. A* **100**, 053401 (2019).
- [44] S. Yamada and K. Yabana, Determining the optimum thickness for high harmonic generation from nanoscale thin films: An *ab initio* computational study, *Phys. Rev. B* **103**, 155426 (2021).
- [45] M. Noda, S. A. Sato, Y. Hirokawa, M. Uemoto, T. Takeuchi, S. Yamada, A. Yamada, Y. Shinohara, M. Yamaguchi, K. Iida *et al.*, Salmon: Scalable *ab initio* light-matter simulator for optics and nanoscience, *Comput. Phys. Commun.* **235**, 356 (2019).
- [46] G. F. Bertsch, J.-I. Iwata, A. Rubio, and K. Yabana, Real-space, real-time method for the dielectric function, *Phys. Rev. B* **62**, 7998 (2000).
- [47] T. Otobe, M. Yamagiwa, J.-I. Iwata, K. Yabana, T. Nakatsukasa, and G. F. Bertsch, First-principles electron dynamics simulation for optical breakdown of dielectrics under an intense laser field, *Phys. Rev. B* **77**, 165104 (2008).
- [48] S. Yamada and K. Yabana, Symmetry properties of attosecond transient absorption spectroscopy in crystalline dielectrics, *Phys. Rev. B* **101**, 165128 (2020).
- [49] M. Uemoto, Y. Kuwabara, S. A. Sato, and K. Yabana, Nonlinear polarization evolution using time-dependent density functional theory, *J. Chem. Phys.* **150**, 094101 (2019).
- [50] A. Yamada and K. Yabana, Energy transfer from intense laser pulse to dielectrics in time-dependent density functional theory, *Eur. Phys. J. D* **73**, 87 (2019).
- [51] M. Schultze, K. Ramasesha, C. Pemmaraju, S. Sato, D. Whitmore, A. Gandman, J. S. Prell, L. J. Borja, D. Prendergast, K. Yabana *et al.*, Attosecond band-gap dynamics in silicon, *Science* **346**, 1348 (2014).
- [52] G. Wachter, C. Lemell, J. Burgdörfer, S. A. Sato, X.-M. Tong, and K. Yabana, *Ab Initio* Simulation of Electrical Currents Induced by Ultrafast Laser Excitation of Dielectric Materials, *Phys. Rev. Lett.* **113**, 087401 (2014).
- [53] N. Troullier and J. L. Martins, Efficient pseudopotentials for plane-wave calculations, *Phys. Rev. B* **43**, 1993 (1991).
- [54] J. P. Perdew and A. Zunger, Self-interaction correction to density-functional approximations for many-electron systems, *Phys. Rev. B* **23**, 5048 (1981).

- [55] G. Onida, L. Reining, and A. Rubio, Electronic excitations: density-functional versus many-body green's-function approaches, *Rev. Mod. Phys.* **74**, 601 (2002).
- [56] C. A. Ullrich, *Time-Dependent Density-Functional Theory: Concepts and Applications*, Oxford Graduate Texts (Oxford University Press, New York, 2012).
- [57] G. Vignale and W. Kohn, Current-Dependent Exchange-Correlation Potential for Dynamical Linear Response Theory, *Phys. Rev. Lett.* **77**, 2037 (1996).
- [58] K. Yabana and G. F. Bertsch, Time-dependent local-density approximation in real time, *Phys. Rev. B* **54**, 4484 (1996).
- [59] S. Plimpton, Fast parallel algorithms for short-range molecular dynamics, *J. Comput. Phys.* **117**, 1 (1995).
- [60] F. H. Stillinger and T. A. Weber, Computer simulation of local order in condensed phases of silicon, *Phys. Rev. B* **31**, 5262 (1985).